Investigation of the aerodynamic characteristics of horizontal axis wind turbine using an active flow control method via boundary layer suction

Peilin Wang[a], Qingsong Liu[a] , Chun Li[a, b], Weipao Miao[a, b, *], Minnan Yue[a], Zifei Xu[a, c]

[a] *School of Energy and Power Engineering, University of Shanghai for Science and Technology, Shanghai, 200093. China*

[b] *Shanghai Key Laboratory of Multiphase Flow and Heat Transfer in Power Engineering, Shanghai 200093, China*

[c] *Liverpool Logistics, Offshore and Marine (LOOM) Research Institute, Liverpool John Moores University, Liverpool, Byrom Street, L3 3AF, UK*

Abstract: The boundary layer suction (BLS) has the merit of effectively suppressing the formation and development of separation vortices by removing low-momentum fluid occurs on the leading-edge of airfoil suction surface. The present paper numerically investigates the impacts of BLS on the aerodynamic performance of a horizontal axis wind turbine (HAWT). First, the dynamic mode decomposition method is adopted to gain an insight into the improvement mechanism of BLS control by analyzing the flow patterns of a two-dimensional S809 airfoil. Subsequently, the BLS is arranged on a NREL Phase VI reference turbine to study the power increment and flow field characteristics, and the effects of different working angles α_s and momentum coefficients C_μ are investigated at different tip speed ratios (TSRs). The results indicate that the use of BLS control can increase the pressure difference between the suction surface and the pressure surface, raise the peak negative pressure at the leading edge and shift the airfoil flow separation point backwards, and thus effectively enhance the stability of the flow field. Furthermore, the BLS control can significantly improve the power extraction at low to medium TSR if this active device is appropriately implemented on the HAWT.

Keywords: Aerodynamic performance; HAWT; computational fluid dynamics; active control; boundary layer suction

1. Introduction

Low-carbon clean energy technologies can effectively mitigate climate change brought by the use of traditional fossil energy sources, and the large-scale promotion of renewable energy is the key to achieving a low-carbon energy transition [1]. Wind energy is viewed as having great potential in promoting the renewable energy and achieving a low-carbon energy transition due to its large storage capacity, non-pollution and renewable advantages [2-4]. According to the Global Wind Report 2022 [5], cumulative global wind power capacity reached 837 GW. In 2021, 93.6 GW of capacity was installed, showing year -over -year growth of 12%. The global offshore wind market enjoyed its best year ever, with 21.1 GW commissioned, which represents three times more than the previous year. Wind turbines, as the largest rotating machines, convert wind energy into mechanical energy, and thus into electricity [6]. Nowadays, two forms of wind turbines are widely accepted: horizontal axis wind turbines (HAWTs) and vertical axis wind turbines (VAWTs) [7]. Distinguished from VAWT, which started late and lagged behind in research, the HAWT is the mainstream of modern large-scale commercial wind turbines due to its technical maturity and high wind energy utilization coefficient [8]. The flow separation phenomenon that occurs during the operation of wind turbines is an important factor affecting the aerodynamic performance of the wind turbine [9]. The resulting unsteady flow will lead to the fluctuation of aerodynamic load, thus reducing the lifetime of wind turbine blade [10]. Due to the large separation flow and transitional geometry, the root of HAWT blade contributes less to the total power generation than the top of the blade, and the aerodynamic loss is more than half of the total aerodynamic loss of the blade [11].

Therefore, the use of flow control techniques to mitigate separated flows is important for the improvement of aerodynamic performance and lifetime of the blade. Flow separation is usually controlled by passive flow control (PFC) or active flow control (AFC) [12]. PFC and AFC are widely used in aircraft wings [13], wind turbines [14], and turbomachinery [15], etc.

PFC includes vortex generators [16], slots [17], gurney flap [18], movable flaps [19], and serrated trailing edges

Corresponding author: Weipao Miao. Tel: 86 18939889435: E-mail address: mwpusst@163.com

[20], etc. For PFC, although its structure is simple, it is difficult to adjust with the change of working conditions, so the control efficiency is low. Wang et al. [21] arranged micro-cylinders on the leading edge of HAWT blades to improve the aerodynamic efficiency of wind turbine. They found that setting appropriate micro-cylinders on the leading edge of blades can effectively suppress the flow separation on the wind turbine blades without increasing the wind turbine load. Moshfeghi et al. [22] analyzed the effect of split position on the aerodynamic performance of HAWT under two wind speeds. The results showed that the aerodynamic performance of the blade was very sensitive to the split position and angle at low tip speed ratios, and its sensitivity decreased as the tip speed ratio increased. Zhang et al. [23] investigated the effect of Gurney flaps arranged on the inner part of the blade at 85% chord location of the pressure surface on the aerodynamic performance of the HAWT. The numerical results show that the arrangement of Gurney flaps can increase the power of the wind turbine by 21% and it has a spanwise effect on the outboard part of the blade.

Different from PFC, AFC mainly improves the local and even global flow field structure through a small range of energy input, which has a large range of adaptive conditions and good control effect. Common AFC includes synthetic jets [24], plasma actuators [25], constant jets [26], and suction devices [27], etc. Abdulrahim et al. [28] studied the effect of tip injection on rotor performance and near-wake characteristics of a HAWT. The experimental results show that tip injection can effectively increase the power and thrust coefficient, and make the boundary between wake and free flow more diffuse. Aono et al. [29] investigated the effect of dielectric barrier discharge plasma actuator (DBD-PA) installed on the leading edge of HAWT on the flow structure, and found that DBD-PA delays the leading edge separation of the blade by affecting the separated leading edge shear layer. Mohammadi et al. [30] studied the effects of multi air jet blowing on aerodynamic performance and torque of HAWT blades at different velocity ratios. It is found that the jets in blade outer part has the greatest influence on the aerodynamic performance of the wind turbine and can produce the highest torque increment. Shi et al. [31] proposed a new AFC called Co-Flowing Jet (CFJ), and studied it for three-dimensional numerical simulation of HAWT aerodynamic performance. The study shows that the deployment of CFJ on the suction surface of the blade can effectively delay the separation, and the power raised by the wind turbine is much higher than the power consumed by CFJ.

The above control forms will change the aerodynamic shape and bring structural resistance. However, HAWT is usually operated at a small angle of attack (AOA), and the jet or the addition of passive control devices may bring adverse effects. While boundary layer suction (BLS) control has good effect in improving aerodynamic efficiency, another important application of BLS control is drag reduction. In 1904, Prandtl [32] initial investigate the BLS as a kind of AFC to control the flow separation occurs on a cylinder. Since then, a number of scholars applied BLS to fluid machines such as aircraft [33], automobiles [34] and wind turbines [38-46].

Wang et al. [35] performed suction control on a thin flat plate airfoil at Re=6.7×10^4, by means of force and velocity field measurements, they found that a suction momentum coefficient of lower than 3% can increase the maximum lift coefficient of this airfoil by about 65% and delay the maximum stall AOA by about 9° in the post stall region. Lei et al. [36] investigated the effect of suction control on the NACA2415 airfoil laminar separation bubble at low Re using a γ-$Re_{\theta t}$ transition model and k-ω turbulence model, and the simulation results showed that the suction control can effectively suppress the flow separation. Meanwhile, the closer the suction position is to the separation bubble and the faster the suction velocity is, the better the control effect is. Arunraj et al. [37] conducted experiments on the effectiveness of airfoil suction control in a wind tunnel and proved that suction control shows better performance at low suction pressures and small AOA, and that maximum lift coefficients can be obtained by performing suction control at 70% of the chord length (c).

The aforementioned researches have only investigated suction control in two-dimensional (2D) airfoil sections, which confirmed the value of suction control for effective delayed separation, but have not been applied to whole-machine simulations or considered three-dimensional (3D) effects. Table 1 summarizes some of the significant work

published in research on the application of suction control in wind turbines.

Table 1

Study of the application of suction control in wind turbines

References	Type of wind turbine	Method	Contribution
Morgulis et al. [38] 2016	VAWT	Experiment	The VAWT with periodic suction is beneficial to the increase of wind energy utilization coefficient at both high and low wind speeds. The VAWT efficiency can be increased by up to 30% at a low tip velocity ratio maximally.
Rezaeiha et al. [39, 40] 2019	VAWT	CFD (2D)	The suction amplitude of 0.5% is sufficient to inhibit the flow separation on the VAWT surface. The position of the suction slit at the leading edge has better effect.
Rezaeiha et al. [41] 2020	VAWT	CFD (2D)	The dynamic stall can be avoided with minimal suction amplitude when the suction slit is located within the chordal range of the separator bubble. The use of unsteady suction can reduce energy consumption and thus increases net power.
Sun et al. [42] 2020	VAWT	CFD (2D)	At a tip speed ratio of 2.33, a suction control with a momentum coefficient of 0.0075 can increase the VAWT power coefficient by 34.25%.
Sun et al. [43]2021	VAWT	CFD (2D)	Influenced by the airfoil separation point and the point of maximum curvature, the best suction point moves with the position of the maximum thickness along the chord towards the trailing edge. When the total suction momentum coefficient is kept constant and the suction slit at 0.3c from the leading edge of the airfoil, the power coefficients with both suction slits blades are higher than those of single.
Arnold et al. [44] 2018	HAWT	CFD (3D)	A maximum reduction of 2.5 dB in trailing edge noise for a 2% increase in maximum wind turbine power coefficient. Up to 3.2 dB reduction in trailing edge noise when power coefficient is not considered.
Arnold et al. [45] 2018	HAWT	CFD (3D)	When using suction control, the high noise reduction requirements can compromise the aerodynamic performance of the wind turbine.
Moussavi et al.	HAWT	CFD (3D)	With suction slits on the inside of the blades and suction

[46] 2021		control applied, the power coefficient of the wind turbine can be increased by 8.1%.

For the study of BLS control, most of the studies in wind turbine airfoil and VAWT have been conducted in 2D methods. However, HAWT has obvious 3D effect [47], and previous results in 2D studies may not be applicable. At the same time, the few studies on BLS control on HAWT only focus on its excellent noise reduction performance, or analyze its control effect under a single tip speed radio (TSR). Different from previous studies, in this research, the dynamic mode decomposition method is firstly adopted to decompose the airfoil with BLS, and analyze the mode and characteristic value unit circle of each order of the flow field to gain an insight into the mechanism of BLS. Then, we studied the power increment effect of BLS arranged at 0.15*c* from the leading edge on HAWT under four TSR, and comprehensively evaluated the BLS control by analyzing the flow field morphology and start-up parameters under the consideration of the energy consumption of BLS. Finally, the effect of BLS working angle on its performance is analyzed. Under the trend of wind turbine shifting from onshore to offshore and from miniaturization to large-scale, it is no longer satisfied to use PFC to perform flow control. BLS control, as a mature flow control technique of AFC, has achieved good results in the field of aviation, so it's very necessary for its application research in HAWT. BLS control is expected to become an effective means to control flow separation of HAWT blades. In this context, the application of BLS in HAWT is completely studied in this paper, in order to provide a certain theoretical basis for the application of BLS in HAWTs.

2. Method and verification

2.1 Geometric model and main aerodynamic parameters

A series of experiments of wind turbine developed and tested by the National Renewable Energy Laboratory (NREL) in the NASA Ames wind tunnel (with a 120 m×80 m closed test section) are widely accepted. Among them, NREL Phase VI HAWT, as one of the experiments providing the most comprehensive data, has been used by a large number of researchers [48-50]. Therefore, the NREL Phase VI HAWT blade is used as the basic model in this research. The wind turbine has a diameter of 10.058 m and a rated power of 19.8 kW [51-53]. The model uses the S809 airfoil at all span positions except for the root (0-1.257 m). After 25% span, the torsion is zero. Table 2 shows details of the geometrical parameters of the wind turbine under study and Fig.1 shows the parameters of blade model.

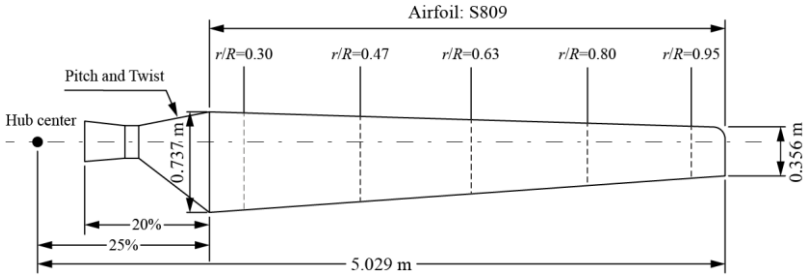

(a) Parameters of the blade model.

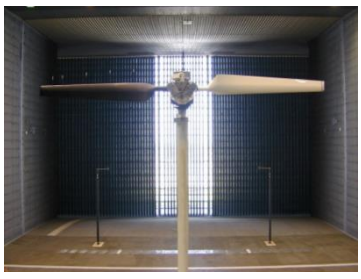

(b) HAWT in NASA wind tunnel [51]

Fig.1. Parameters of NREL Phase VI wind turbine blade model.

Table 2

Geometrical parameters of the NREL Phase VI wind turbine

Property [Symbol]	Unit	Value
Rated power [P_R]	kW	19.8
Cut-in wind speed [V_{in}]	m/s	5
Cut-out wind speed [V_{out}]	m/s	25
Rotor diameter [D_r]	m	10.058

Hub height [H_r]	m	12.192
Cone angle [α_c]	°	0
Pitch angle [β]	°	5

In this experiment, through the variable-speed control of fans and the variable-pitch control of fan blade, the velocities in the test section can be accurately controlled from 0 m/s to 50 m/s. The rotor operates at a nominal 72 RPM. The time-series measurements for this test were obtained by the NREL data system, which was limited by experimental uncertainty. Among them, the uncertainty of velocity measurement is about 1%, while for the pressure measurement can be estimated as 0.05%, among which the wall pressure is 0.03%. In addition, the turbine blockage was found to be less than 1%.

2.2 BLS model

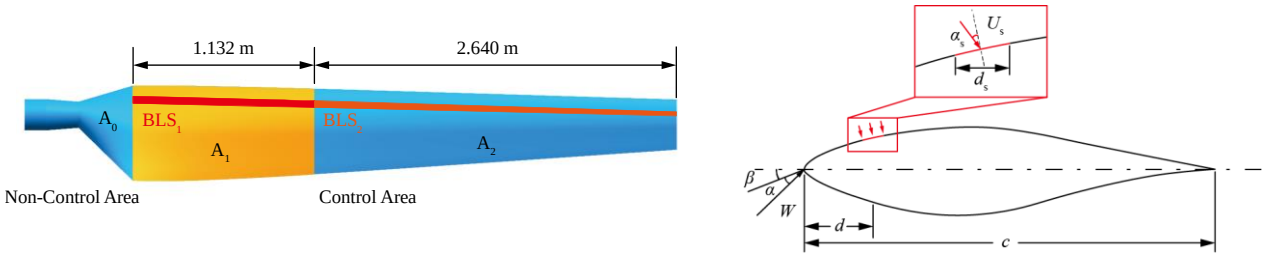

(a) 3D-BLS model (b) 2D-BLS model

Fig.2. The 3D-BLS model and 2D-BLS blade section model.

Modeling of the clean blade and BLS blade by using UG NX12.0, layout of BLS from the 25% span. The control area is divided into two parts, A_1 (root of the blade) in the first 1.132 m and A_2 (middle and tip of the blade) in the second 2.640 m. The 3D-BLS model and 2D-BLS blade section model are shown in Fig.2. In the figure, α_s is the working angle of the BLS, °; d_s is the width of the BLS, m; U_s is the velocity of the BLS, m/s; d is the distance of the BLS from the leading edge, m; c is the chord length of airfoil at this section, m. It is worth noting that the BLS width narrows as the chord length of the spreading section decreases, but possesses a constant ratio of 0.02c.

The suction momentum coefficient (C_μ) is chosen as a parameter to measure the quantification of suction control, which is defined as:

$$C_\mu = 2\dot{m}V_R / \rho_\infty U_\infty c \tag{1}$$

where $\dot{m}$ is the mass flow rate of BLS working gas, kg/s and the V_R is the velocity ratio, which is defined as:

$$\dot{m} = A_s \cdot U_s \cdot \rho_s \tag{2}$$

$$V_R = U_s / U_\infty \tag{3}$$

where A_s is the area of the BLS, m^2; ρ_s is the density of the working gas, kg/m^3.

As a type of AFC, this research introduces energy consumption (P_{BLS}) as a measure of loss, which is defined as:

$$P_{BLS} = \frac{\dot{m}c_p T_s}{\eta_s}\left[\left(\frac{p_\infty}{p_s}\right)^{\frac{\gamma-1}{\gamma}} - 1\right] \tag{4}$$

where c_p is the constant pressure specific heat capacity, kJ/(kg·K); T_s is the total temperature of the BLS, which is 298.15 K; η_s is the efficiency of pump, which is 80%; p_s is the total pressure of the BLS, Pa; γ is the ratio of specific heat, which is 1.4.

3 Computational and numerical method

3.1 Computational domain and meshing

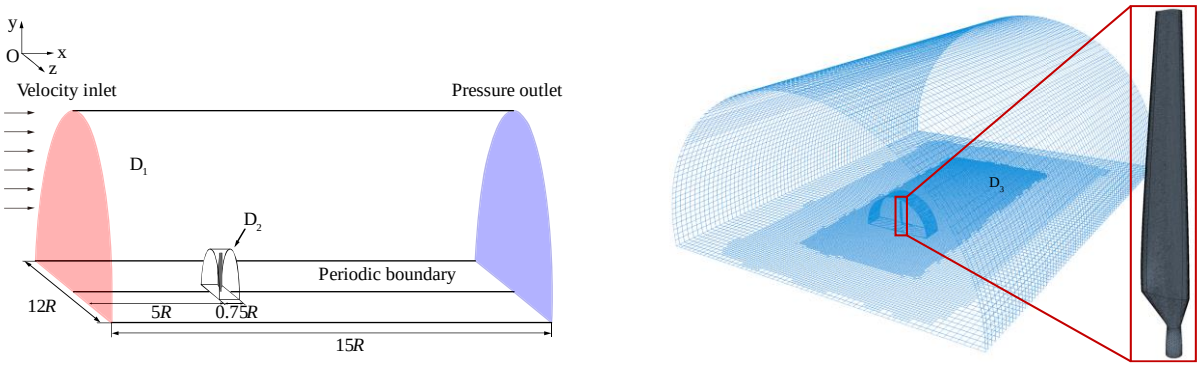

(a) Computational domain (b) Computational mesh

Fig.3. Computational domain and mesh of the wind turbine.

The grid and boundary conditions of wind turbine computing domain are shown in Fig.3. The computational domain is divided into three sub-domains: the Background zone (D_1), the Rotating zone (D_2), and the Overset refine zone (D_3). The mesh density of D_2 and D_3 is higher than the other zones, allowing for more accurate aerodynamic performance calculations and obtaining more precise details of the captured flow field.

The left side of Fig.3a (light red area) is the velocity inlet, and the velocity flow is parallel to x+; the right side (light blue area) is the pressure outlet with a gauge pressure of 0 Pa; rotational periodic boundary conditions are used for the symmetry plane; and no-slip boundary conditions are used for the blade surface. As NREL Phase VI wind turbine has two blades, the model and flow field are periodic, the simulation is carried out for a single blade to reduce computational costs. The rotating speed of the wind rotor is fixed at about 7.2 rad/s. In all simulations, air is assumed to be an incompressible fluid with density ρ_∞=1.185 kg/m^3 and dynamic viscosity μ_∞=1.855×10^{-5} Pa·s.

3.2 Numerical method

In order to simulate the flow field around a HAWT blade, the selection of a suitable turbulence model is essential. For the NREL Phase VI HAWT, the selection of a turbulence model has been studied in depth and detail by many researchers. Jones et al. [54] believed that the *k-ε* model had a good performance in calculating the free flow region (outside the boundary layer). Wilcox [55] demonstrated that the *k-ω* model has good performance in dealing with internal boundary layer by combining numerical calculation with singular disturbance. However, for HAWT, the k-ω and k-ε models cannot simulate the flow around the HAWT blade well due to the large-scale flow separation at the blade root during stall [56-58]. The SST *k-ω* model proposed by Menter [59] in 1994 used the *k-ω* model at the near-wall and the *k-ε* model outside the boundary layer. Tachos et al. [60] compared four turbulence models, which concluded that the SST *k-ω* model is more suitable for simulating NREL Phase VI HAWT. Meanwhile, other researchers also reached similar conclusions [58, 61], this is why the SST *k-ω* turbulence model is adopted in this research for simulation.

For the SST *k-ω* turbulence model, its *k* and *ω* are defined as:

$$\frac{\partial}{\partial x_i}(\rho u_i u_j) = -\frac{\partial}{\partial x_i}(\mu_k \frac{\partial k}{\partial x_i}) + P_k - \rho\beta^* k\omega \tag{5}$$

$$\frac{\partial}{\partial x_i}(\rho\omega u_i) = \frac{\partial}{\partial x_i}(\mu_\omega \frac{\partial \omega}{\partial x_i}) + \frac{\alpha}{\nu_t} P_k - \rho\beta^*\omega^2 + 2(1-F_1)\rho\frac{\sigma_{\omega,2}}{\omega}\frac{\partial k}{\partial x_i}\frac{\partial \omega}{\partial x_i} \tag{6}$$

where μ_k and μ_ω are the effective diffusivities for the turbulent kinetic energy and specific dissipation rate, respectively.

To improve the accuracy of the results, unsteady assumptions are used for the simulations. The discretization method adopts the second order upwind scheme. The simulated time step is set as $T/360$, corresponding to the time that the HAWT rotates by 1° ($\pi/180$). For better convergence, internal iteration of 10 for clean blade and 25 for BLS blade are selected. The convergence of the simulation is checked by monitoring momentum residuals less than 10^{-5}. In addition, the simulation stops when the difference between the average torque value in the current rotation period and the previous rotation period is less than 3%, and the data used below are the average values of the last rotation period.

4. Validation

4.1 Grid independence validation

During the computational fluid dynamics (CFD) calculations, the study of grid independence is indispensable. The Grid Convergence Index (GCI) method proposed by Roache in 1994 is still the common method used today to assess truncation errors [62]. According to the suggestions, we checked by the total number of units (N), with the refinement factors all greater than 1.3. The specific process is as follows:

First define l_g as the grid size:

$$l_g = \left[\frac{1}{N_g} \sum_{i=1}^{N_g} (\Delta V_i) \right]^{\frac{1}{3}} \tag{7}$$

where ΔV_i is the volume of each grid cell; N_g is the total number of ΔV_i units used for calculation, which N_1 is for Fine mesh, N_2 is for Medium mesh and N_3 is for Coarse mesh.

The refinement factor (f) between different grids is defined as:

$$f_{g+1,g} = \frac{l_{g+1}}{l_g} \tag{8}$$

The torque of the HAWT is taken as the key variable and defined as φ_g, and then the difference $\varepsilon_{g+1,g}$ of two similar φ is obtained:

$$\varepsilon_{g+1,g} = \varphi_{g+1} - \varphi_g \tag{9}$$

Then the relative error $e_{g+1,g}$ is obtained:

$$e_{g+1,g} = \left| \frac{\varepsilon_{g+1} - \varepsilon_g}{\varepsilon_g} \right| \tag{10}$$

Calculate the estimate of GCI, which is defined as follows:

$$GCI_{g+1,g} = F_s \frac{e_{g+1,g}}{f_{g+1,g}^p - 1} \tag{11}$$

where F_s is the safety factor, which is suggested in literature [63] to be in the range of 1.25-3.00, and 1.25 is selected in this research. Besides, p is the apparent order, which is defined as:

$$p = \frac{\left| \ln \left| \varepsilon_{32} / \varepsilon_{21} \right| + q(p) \right|}{\ln(f_{21})} \tag{12}$$

Since f is a constant in this research, $q(p)$=0.

Table 3 shows the GCI calculations for three grids (Fine, Medium and Coarse) under three different incoming

wind speeds (10 m/s, 13 m/s, 15 m/s).

Table 3

GCI assessment at different incoming wind speeds

Parameters	Value		
	U_∞=10 m/s	U_∞=13 m/s	U_∞=15 m/s
N_1	4894310	4894310	4894310
N_2	3516274	3516274	3516274
N_3	2634810	2634810	2634810
f_{32}	1.49	1.49	1.49
f_{21}	1.49	1.49	1.49
φ_1	663.930	1280.125	1044.752
φ_2	661.449	1274.388	1043.219
φ_3	630.588	1259.216	1023.541
ε_{32}	-30.861	-15.172	-19.678
ε_{21}	-2.481	-5.737	-1.533
F_s	1.25	1.25	1.25
e_{32}	4.66567%	1.19053%	1.88628%
e_{21}	0.03266%	0.27177%	0.01240%
GCI_{32}^{Medium}	0.50984%	0.90489%	0.19921%
GCI_{21}^{Fine}	0.04083%	0.34063%	0.01550%

It can be seen that the convergence of the three grids (N_1, N_2, N_3) is monotonically decreasing for all three incoming wind speeds. The specific performance is 0.510% and 0.041% for GCI_{32}^{Medium} and GCI_{21}^{Fine} under U_∞=10 m/s, respectively; 0.905% and 0.341% under U_∞=13 m/s, respectively; 0.199% and 0.016% under U_∞=15 m/s, respectively. And the maximum value of GCI_{21}^{Fine} is 0.341%, which is less than 1% and has good convergence. This means that the Medium mesh is already sufficiently accurate and increasing the amount of mesh is a very small improvement in accuracy. Therefore, Medium mesh is selected as the computational mesh in this research.

4.2 Pressure coefficient validation

The pressure coefficient (C_p) of the blade cross section along the spanwise direction is defined as:

$$C_p = \frac{2(p_0 - p_\infty)}{\rho_\infty \left(U_\infty^2 + (r\omega)^2\right)} \tag{13}$$

where p_0 is the surface pressure, Pa; p_∞ is the flow pressure, Pa; U_∞ is the incoming flow speed, m/s; r is the radial distance of local spanwise station, m; ω is the angular velocity of the rotor, rad/s.

U_∞=7 m/s U_∞=15 m/s U_∞=25 m/s

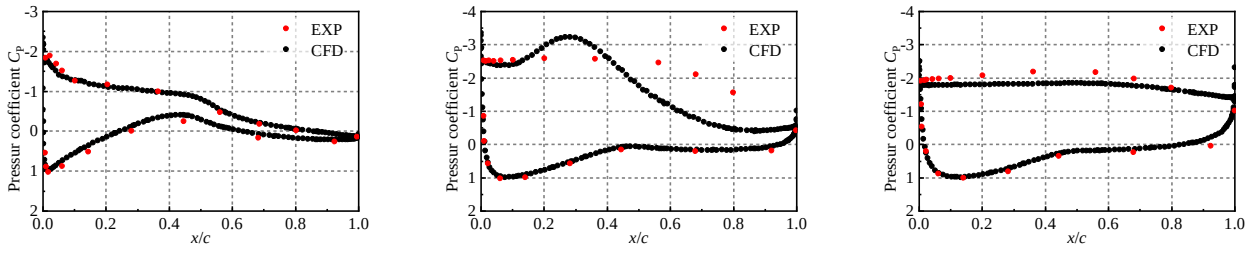

(a) r/R=0.30

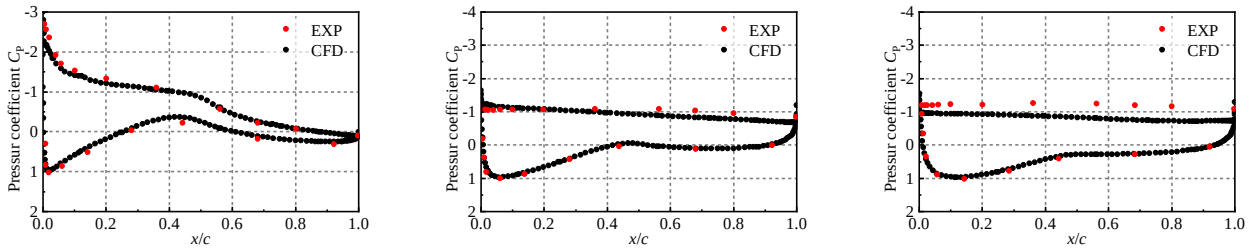

(b) r/R=0.47

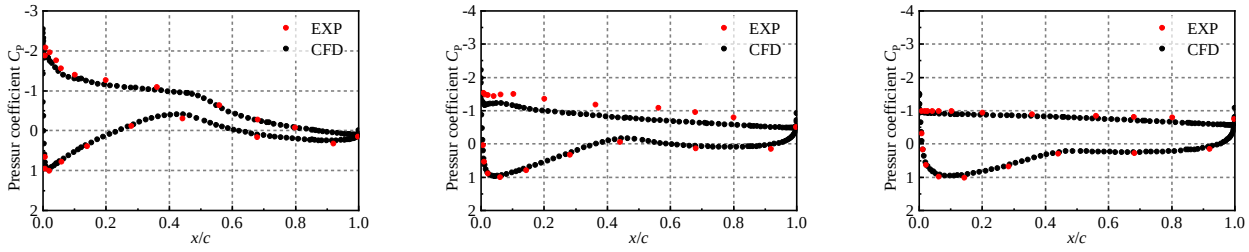

(c) r/R=0.63

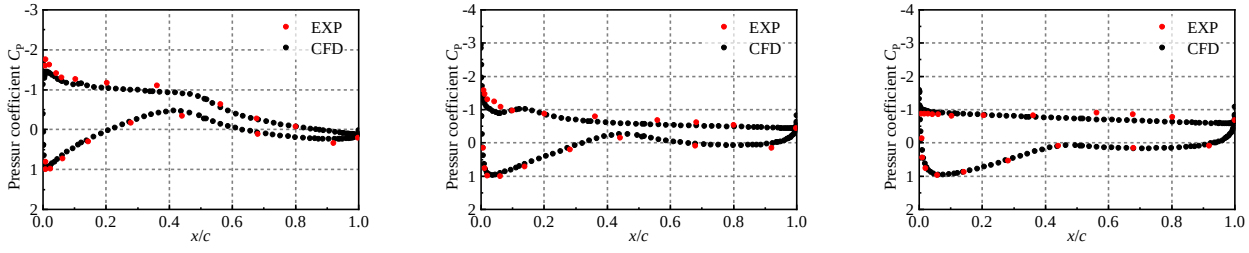

(d) r/R=0.80

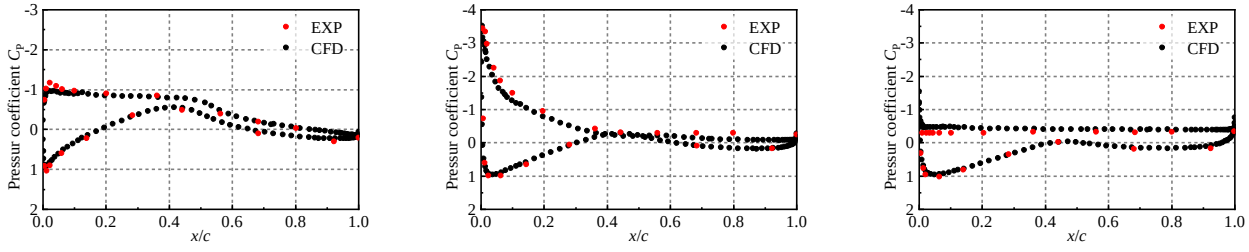

(e) r/R=0.95

Fig.4. Pressure coefficient compared with experiment.

Since the experimental incoming flow speed ranges from 5 m/s to 25 m/s, according to its given data, this research selects representative surface pressure coefficients of five blade sections under three U_∞ for comparison. At a U_∞ of 15 m/s and r/R=0.30, our results appear to deviate from the estimate of the pressure coefficient on the suction surface, with a good pressure surface match. This should be due to the fact that our results overestimate the stall at the leaf root when U_∞=15 m/s and its effect on the aerodynamic properties of the blade. Similar results exist in previous calculations by other researchers [64, 65, 49].

In addition, the pressure coefficients at r/R=0.30, 0.47, 0.63, 0.80 and 0.95 when the U_∞=7 m/s, 15 m/s and 25 m/s are in high agreement with the experimental values. This indicates that the turbulence model selection and meshing in this research have high accuracy.

4.3 Torque validation

An important factor in assessing the aerodynamic performance of a wind turbine is the torque (T), which is defined as:

$$T = \rho_\infty A U_d (U_\infty - U_w) \tag{14}$$

where A is the swept area of wind turbine, m^2; U_d is the axial velocity of flow through the wind turbine, m/s; U_w is the downstream speed of wind turbine, m/s.

Output power of wind turbine (P) can be calculated by torque:

$$P = TU_d \tag{15}$$

Further define the power coefficient (C_P) as:

$$C_P = \frac{2P}{\rho_\infty A U_\infty^3} \tag{16}$$

The relative error is calculated as follows:

$$E = \frac{T_{Exp} - T_{Cal}}{T_{Exp}} \times 100 \tag{17}$$

where T_{Exp} is the torque of the experiment; T_{Cal} is the torque calculated by CFD.

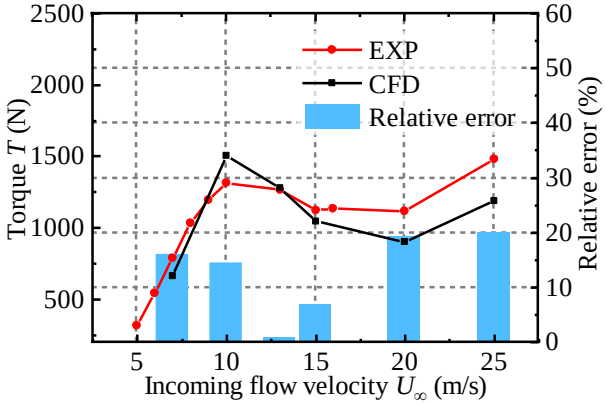

Fig.5. Comparison of experimental and CFD result of torque

Fig.5 shows a comparison of the torque curves between the EXP data and the CFD results. As can be seen from the figure, there is a high degree of similarity between our results and the experimental results, and the relative errors are all less than 20%. This indicates that our calculations can accurately predict the power of the wind turbine under various stall conditions (pre-stall, stall, and post-stall). The highest degree of agreement is found when U_∞=13 m/s, where the relative error is only 0.74%. Besides, since the blade pitch system will operate at high wind speeds, this research chooses to analyze the blade controlled by BLS when U_∞=7, 10, 13 and 20 m/s. TSR and relative velocity of each section of selected U_∞ are shown in Table 4.

Table 4

TSR and relative velocity of each section at different incoming wind speeds

Incoming wind speeds (m/s)	TSR	Relative velocity (m/s)				
		r/R=0.30	r/R=0.47	r/R=0.63	r/R=0.80	r/R=0.95
7	5.4	13.36	19.15	24.89	31.13	36.70
10	3.8	15.15	20.44	25.90	31.94	37.38
13	2.9	17.27	22.06	27.20	33.00	38.30
20	1.9	23.01	26.79	31.16	36.33	41.20

The TSR of HAWT blade is a very important parameter for expressing the wind turbine characteristics, which is defined as:

$$\lambda = \frac{\omega R}{U_\infty} \tag{18}$$

where R is the rotor radius, m.

5. Results and discussions

5.1 Dynamic mode decomposition analysis of the S809 airfoil with BLS control

The flow field mode decomposition method is an analytical method that extracts the main features of the flow field and simplifies it. Typical methods of flow field mode analysis are the principal orthogonal decomposition (POD) and the dynamic mode decomposition (DMD) [66].

The DMD algorithm is based on a linear operator that best fits the dynamic properties of the flow field, decomposing the flow field into a number of modes with a single characteristic frequency and growth/decay rate. Therefore, DMD can obtain the contribution of different frequency flow structure to the flow field.

For an in-depth analysis of the BLS control mechanism, a DMD analysis of the 2D BLS airfoil is first carried out. It takes the section at 75% span, where the line length c is 0.483 m, under a relative velocity of 29.29 m/s. The BLS is arranged at 0.15c from the leading edge of the airfoil with C_μ=0.01.

For flow field variable information, assume that there exists a matrix $\boldsymbol{A}$ such that there is a linear mapping between adjacent time layers $\boldsymbol{u}_{i+1}$ and $\boldsymbol{u}_i$.

$$\boldsymbol{u}_{i+1} = \boldsymbol{A}\boldsymbol{u}_i \tag{19}$$

Defining $\boldsymbol{\psi}_0 = [\boldsymbol{u}_1, \boldsymbol{u}_2, \cdots, \boldsymbol{u}_{N-1}]$, $\boldsymbol{\psi}_1 = [\boldsymbol{u}_2, \boldsymbol{u}_3, \cdots, \boldsymbol{u}_N]$, the following relation can be given:

$$\boldsymbol{\psi}_1 = \boldsymbol{A}\boldsymbol{\psi}_0 = [\boldsymbol{A}\boldsymbol{u}_1, \boldsymbol{A}\boldsymbol{u}_2, \cdots, \boldsymbol{A}\boldsymbol{u}_{N-1}] \tag{20}$$

For a matrix with rank r_m, usually $\boldsymbol{A}$ is a high dimensional matrix with a large amount of data. The purpose of DMD algorithm is to replace $\boldsymbol{A}$ with a low dimensional optimization approximation matrix $\tilde{\boldsymbol{A}}$, so that:

$$\boldsymbol{A} = \boldsymbol{U}\tilde{\boldsymbol{A}}\boldsymbol{U}^\mathrm{H} \tag{21}$$

where $\tilde{\boldsymbol{A}}$ is a square matrix of order r, and $\boldsymbol{U}$ can be obtained by singular value decomposition.

Perform a singular value decomposition of $\boldsymbol{\psi}_0$:

$$\boldsymbol{\psi}_0 = \boldsymbol{U}\boldsymbol{S}\boldsymbol{V}^\mathrm{H} \tag{22}$$

where $\boldsymbol{U}$ is a $M \times r_\mathrm{m}$ left orthogonal matrix; $\boldsymbol{S}$ is a $r_\mathrm{m} \times r_\mathrm{m}$ singular value diagonal matrix; $\boldsymbol{V}$ is a $r_\mathrm{m} \times N$ right orthogonal matrix; the superscript H denotes the complex conjugate transpose, which in turn leads to the approximation matrix:

$$\boldsymbol{A} \approx \tilde{\boldsymbol{A}} = \boldsymbol{U}^\mathrm{H}\boldsymbol{\psi}_1\boldsymbol{V}\boldsymbol{S}^{-1} \tag{23}$$

The DMD mode is defined as follows:

$$\boldsymbol{\varphi}_i = \boldsymbol{\psi}_1\boldsymbol{V}\boldsymbol{S}^{-1}\boldsymbol{y}_i \tag{24}$$

where $\boldsymbol{y}_i$ is the eigenvector of the low-dimensional approximation matrix $\tilde{\boldsymbol{A}}$.

The eigenvalues and eigenvectors of the matrix $\boldsymbol{S}$ are given by Eq. (22) as:

$$\boldsymbol{S}\boldsymbol{y}_i = \mu_i \boldsymbol{y}_i \tag{25}$$

where μ_i is a complex number, its real part expresses the growth rate of the corresponding mode and the imaginary part contains the frequency information.

When performing stability analysis of modes, a positive growth rate indicates that the corresponding mode is

unstable, a negative growth rate indicates that the corresponding mode is stable and a zero growth rate indicates that the corresponding mode is periodic. This method allows for a quantitative determination of the stability of a mode.

Another way of determining stability is to observe the distribution of eigenvalues on the unit circle, with the horizontal axis being the real part of the eigenvalue and the vertical axis being the imaginary part of the eigenvalue. If the eigenvalue corresponds to a point outside the unit circle, then its magnification is positive, corresponding to an unstable mode; if the eigenvalue corresponds to a point inside the unit circle, then its magnification is negative, corresponding to a stable mode; if the eigenvalue corresponds to a point on the unit circle, then the magnification is zero, corresponding to a periodic mode.

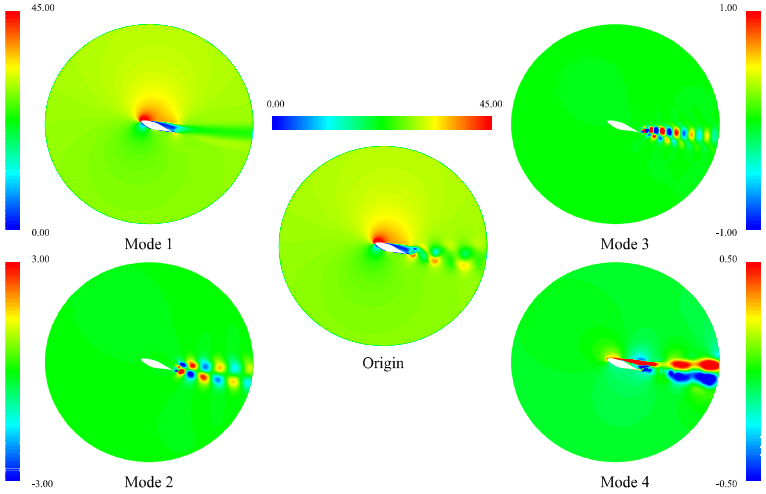

(a) Mode of clean airfoil

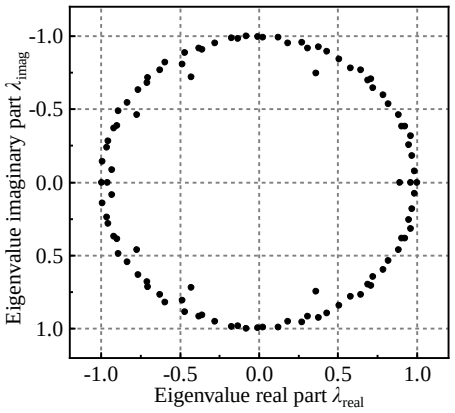

(b) Eigenvalue of clean airfoil

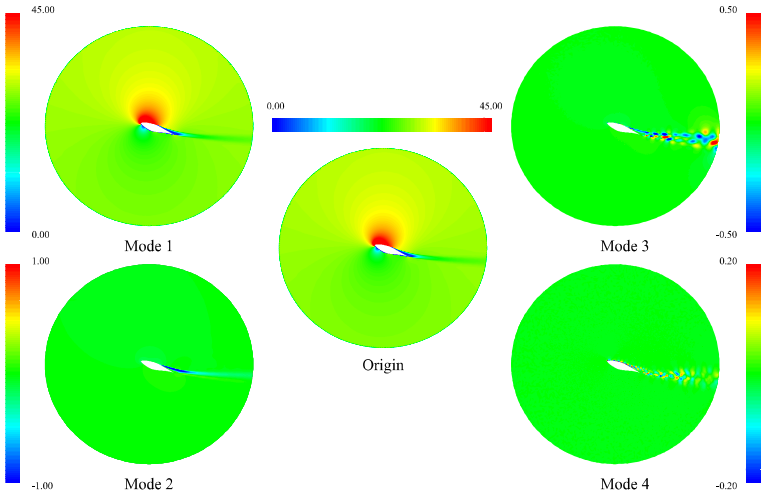

(c) Mode of BLS airfoil

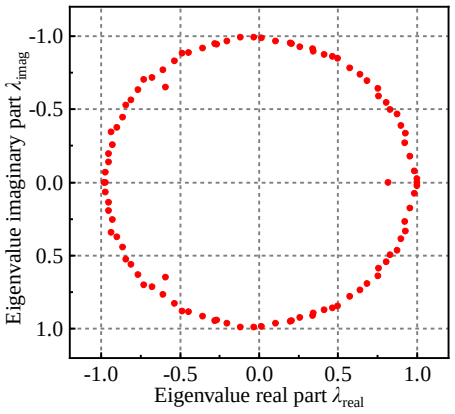

(d) Eigenvalue of BLS airfoil

Fig.6. Mode and the eigenvalue of clean airfoil and BLS airfoil.

As can be seen in Fig.6a and 6c, at an AOA of 20°, the clean airfoil shows alternating vortex shedding at the trailing edge. The Mode 1 reflects the mean flow field and shows a large stall area at the suction surface of the clean airfoil, while the BLS airfoil shows a significantly reduced stall area due to the better fluid attachment at the suction surface by inhaling low-momentum fluid in the boundary layer. The main structure of Mode 2 is found in the trailing edge and trailing area: the fluctuating structure of Mode 2 of the clean airfoil forms a bilayer structure with upper and lower symmetry in the trailing area; Mode 2 of the BLS airfoil is mainly found in the small stall area at the trailing edge. Mode 3 and 4 are small-scale complex flows captured by the DMD. Obviously, the fluctuation range and amplitude of BLS airfoil are much smaller than that of clean airfoil.

Further observe the distribution of the characteristic values of clean airfoil and BLS airfoil on the unit circle. As

seen in Fig.6b and 6d, clean airfoil has 5 pairs of characteristic values outside the unit circle, while BLS airfoil only has 3 pairs. Compared with clean airfoil, the characteristic values of BLMS airfoil are closer to the unit circle, which indicates that BLMS control can effectively increase the stability of flow field.

5.2 Effect of different momentum coefficients on power increment

Fixing the position of BLS control at 0.15c from the leading edge, we simulated the improvement of BLS control on the work capacity of HAWT with different momentum coefficients at four incoming wind speeds (U_∞=7, 10 13 and 20 m/s). For each incoming wind speed, 12 cases are set and the results are as follows.

Define $P_{\mathrm{BLS\_Net}}$ as the power increment after considering the BLS energy consumption:

$$P_{\mathrm{BLS\_Net}} = P - P_{\mathrm{Clean}} - P_{\mathrm{BLS}} \tag{26}$$

where P_{Clean} is the power of clean blade, W.

Table 5

Power increment and BLS energy consumption of blades at different C_μ under U_∞=7 m/s

Case	C_μ of BLS_1	C_μ of BLS_2	Power P (W)	Power increment ΔP (W)	P_{BLS} (W)	$P_{\mathrm{BLS\_Net}}$ (W)
L1	0.04	0.00	2566.05	72.45	92.30	-19.85
L2	0.09	0.00	2598.80	105.19	138.45	-33.26
L3	0.16	0.00	2637.23	143.63	184.60	-40.97
L4	0.00	0.04	2923.39	429.79	221.33	208.46
L5	0.00	0.09	3039.26	545.65	332.00	213.66
L6	0.00	0.16	3174.42	680.82	442.66	238.16
L7	0.01	0.01	2821.12	327.52	156.82	170.71
L8	0.02	0.02	2896.93	403.33	221.77	181.56
L9	0.04	0.04	3014.60	520.99	313.63	207.36
L10	0.09	0.09	3163.38	669.77	470.44	199.33
L11	0.16	0.16	3308.91	815.31	627.26	188.05
L12	0.25	0.25	3462.14	968.53	784.07	184.46

Table 6

Power increment and BLS energy consumption of blades at different C_μ under U_∞=10 m/s

Case	C_μ of BLS_1	C_μ of BLS_2	Power P (W)	Power increment ΔP (W)	P_{BLS} (W)	$P_{\mathrm{BLS\_Net}}$ (W)
S1	0.04	0.00	5870.09	200.92	240.60	-39.68
S2	0.09	0.00	5949.42	280.25	360.90	-80.65
S3	0.16	0.00	6038.04	368.87	481.20	-112.33
S4	0.00	0.04	6256.11	586.94	562.66	24.28
S5	0.00	0.09	6580.81	911.63	843.99	67.65
S6	0.00	0.16	6980.39	1311.22	1125.32	185.90
S7	0.01	0.01	7053.40	1384.22	401.63	982.59
S8	0.02	0.02	7251.30	1582.12	567.96	1014.17
S9	0.04	0.04	7500.69	1831.52	803.26	1028.26
S10	0.09	0.09	7847.85	2178.68	1204.89	973.79
S11	0.16	0.16	8216.73	2547.56	1606.51	941.05

S12	0.25	0.25	8612.87	2943.70	2008.14	935.55

Table 5-6 show the energy increment and BLS energy consumption of blades at different C_μ under U_∞=7 m/s and 10 m/s. As can be seen from Table 5, under U_∞=7 m/s, BLS control has a very weak power increment effect of blade, and the maximum improvement is only about 230 W. And when only BLS_2 works, the power increment is greater than when BLS_1 and BLS_2 work at the same time. When the C_μ of BLS_2 is 0.16, the P_{BLS_Net} is highest at 238.16 W.

As can be seen from Table 6, when BLS_1 works and BLS_2 shuts down, its effect on power increment of blade is limited. After taking into account BLS energy consumption, the gain is negative. Interestingly, as the momentum coefficient increases, its negative gain increases. When BLS_1 shut down and BLS_2 works, it has obvious effect on power increment of blade. After taking into account the P_{BLS}, the gain is still positive. At this point, with the increase of momentum coefficient, its power increment increases However, when both BLS_1 and BLS_2 work, the blade power is significantly increased and the amount of increment is not simply superimposed, but a greater increment. While higher C_μ has a higher power increment, it also comes with a higher P_{BLS}. When the C_μ of BLS_1 and BLS_2 is 0.04, the ΔP-P_{BLS} is highest at 1028.26 W.

Table 7

Power increment and BLS energy consumption of blades at different C_μ under U_∞=13 m/s

Case	C_μ of BLS_1	C_μ of BLS_2	Power P (W)	Power increment ΔP (W)	P_{BLS} (W)	P_{BLS_Net} (W)
M1	0.04	0.00	5375.45	571.12	320.80	250.32
M2	0.09	0.00	4355.58	-448.74	450.41	-899.16
M3	0.16	0.00	4386.67	-417.66	600.5	-1018.21
M4	0.00	0.04	7331.73	2527.40	765.29	1762.12
M5	0.00	0.09	8886.39	4082.06	1147.93	2934.13
M6	0.00	0.16	10866.26	6061.93	1530.58	4531.35
M7	0.16	0.16	14567.93	9763.60	2131.13	7632.47
M8	0.25	0.25	15565.32	10760.99	2663.91	8097.08
M9	0.36	0.36	16420.04	11615.71	3196.70	8419.02
M10	0.49	0.49	17263.90	12459.57	3729.48	8730.10
M11	0.64	0.64	17020.57	12216.24	4262.26	7953.98
M12	0.81	0.81	16621.29	11816.96	4795.04	7021.92

Table 8

Power increment and BLS energy consumption of blades at different C_μ under U_∞=20 m/s

Case	C_μ of BLS_1	C_μ of BLS_2	Power P (W)	Power increment ΔP (W)	P_{BLS} (W)	P_{BLS_Net} (W)
H1	0.04	0.00	4550.28	1162.13	505.26	656.88
H2	0.09	0.00	4216.15	828.01	757.88	70.12
H3	0.16	0.00	4034.83	646.69	1010.51	-363.83
H4	0.00	0.04	6023.16	2635.01	1181.58	1453.43
H5	0.00	0.09	6918.21	3530.07	1772.38	1757.69
H6	0.00	0.16	7513.90	4125.76	2363.17	1762.59
H7	0.16	0.16	8755.05	5366.91	3373.68	1993.23
H8	0.25	0.25	12195.51	8807.37	4217.10	4590.27
H9	0.36	0.36	16090.80	12702.66	5060.52	7642.14
H10	0.49	0.49	16594.22	13206.07	5903.94	7302.13

H11	0.64	0.64	17014.23	13626.09	6747.36	6878.73
H12	0.81	0.81	17398.78	14010.64	7590.78	6419.86

Table 7-8 show the energy increment and BLS energy consumption of blades at different C_μ under U_∞=13 m/s and 20 m/s. The results obtained under U_∞=13 m/s and 20 m/s (Low to medium TSR) are similar to that under U_∞=7 m/s and 10 m/s (High TSR). The difference is that the power increment to the blades with BLS control at low to medium TSR is much greater than that at high TSR. Under U_∞=13 m/s, when the C_μ of BLS_1 and BLS_2 is 0.49, the power of clean blade which is 4804.33 W can be increased by 12459.57 W with BLS control. After considering the P_{BLS}, the increment is still 8730.10 W. Under U_∞=20 m/s, when the C_μ of BLS_1 and BLS_2 is 0.36, the power of clean blade which is 3388.14 W can be increased by 16090.80 W with BLS control. After considering the P_{BLS}, the increment is still 7642.14 W.

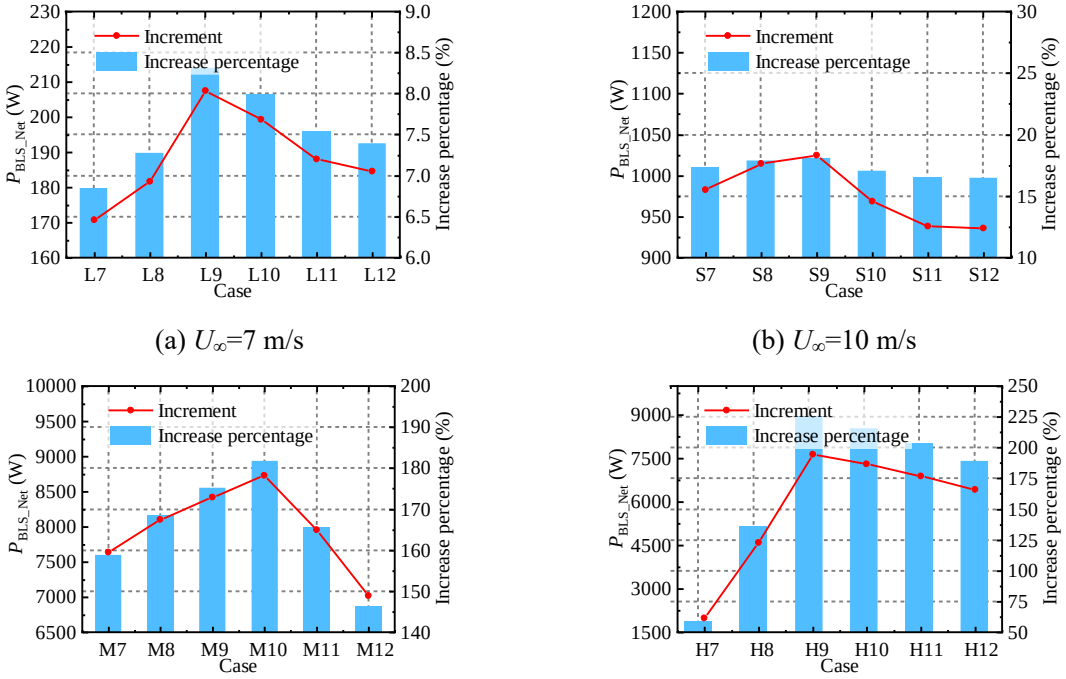

(a) U_∞=7 m/s (b) U_∞=10 m/s

(c) U_∞=13 m/s (d) U_∞=20 m/s

Fig.7. Power increment under U_∞=7, 10, 13 and 20 m/s.

Further analysis of power increment and increase percentage for different BLS momentum coefficients. Fig.7 shows the power increment when BLS energy consumption is considered. As seen in Fig.7a and 7b, under U_∞=7 m/s, the average power increment of BLS blade is 188.58 W. Among them, L9 has the most power increment of 207.36 W, which is 8.32% higher than the clean blade. Under U_∞=10 m/s, the average power increment of BLS blade is 977.39 W. Among them, S9 has the most power increment of 1028.26 W, which is 18.08% higher than the clean blade.

As seen in Fig.7c and 7d, under U_∞=13 m/s, the average power increment of BLS blade is 7975.76 W Among them, M10 has the most power increment of 8730.10 W, which is 181.71% higher than the clean blade. Under U_∞=20 m/s, the average power increment is 5804.39 W. Among them, H9 has the most power increment of 7642.14 W, which is 225.56% higher than the clean blade.

It can be seen that the power increment is not only the result of single control area, but the result of the joint control of both control areas. Although the contribution of BLS_2 to power increment is much greater than that of BLS_1, the role of BLS_1 cannot be ignored, that is, BLS_1 and BLS_2 are indispensable. In addition, the effect of BLS control is better at low to medium TSR than at high TSR.

5.3 Correlations to predict power increment curves of the turbine

In this section, the correlation equations for HAWT with BLS control have been formed to predict the increment percent of the HAWT at different TSRs. For low to medium TSR, the V_R is in the range of 0.5-2.5, while for high TSR, the range of V_R is 2-4.5. The correlation equations to predict increment percent with reference to V_R for different TSR are as follows:

$$P_{BLS\_Net} = 3.30 + 9.54V_R - 5.89V_R^2 + 1.09V_R^3 \quad \text{for TSR} = 5.4;\ 0.5 \le V_R \le 2.5 \tag{27}$$

$$P_{BLS\_Net} = 14.37 + 9.13V_R - 7.03V_R^2 + 1.49V_R^3 \quad \text{for TSR} = 3.8;\ 0.5 \le V_R \le 2.5 \tag{28}$$

$$P_{BLS\_Net} = 165.53 - 48.42V_R + 32.63V_R^2 - 5.08V_R^3 \quad \text{for TSR} = 2.9;\ 2.0 \le V_R \le 4.5 \tag{29}$$

$$P_{BLS\_Net} = -1084.58 + 945.35V_R - 220.83V_R^2 + 16.34V_R^3 \quad \text{for TSR} = 1.9;\ 2.0 \le V_R \le 4.5 \tag{30}$$

Fig. 8 show the correlations between increment percent and V_R at different TSR. In the curve fitting process, third degree polynomials have been fitted through the data points, which give a very high R-squared value, except for TSR=5.4. It is worth noting that the relevant equation derived in this paper has some limitations, and the equation only has a good fit in the V_R range at a certain TSR.

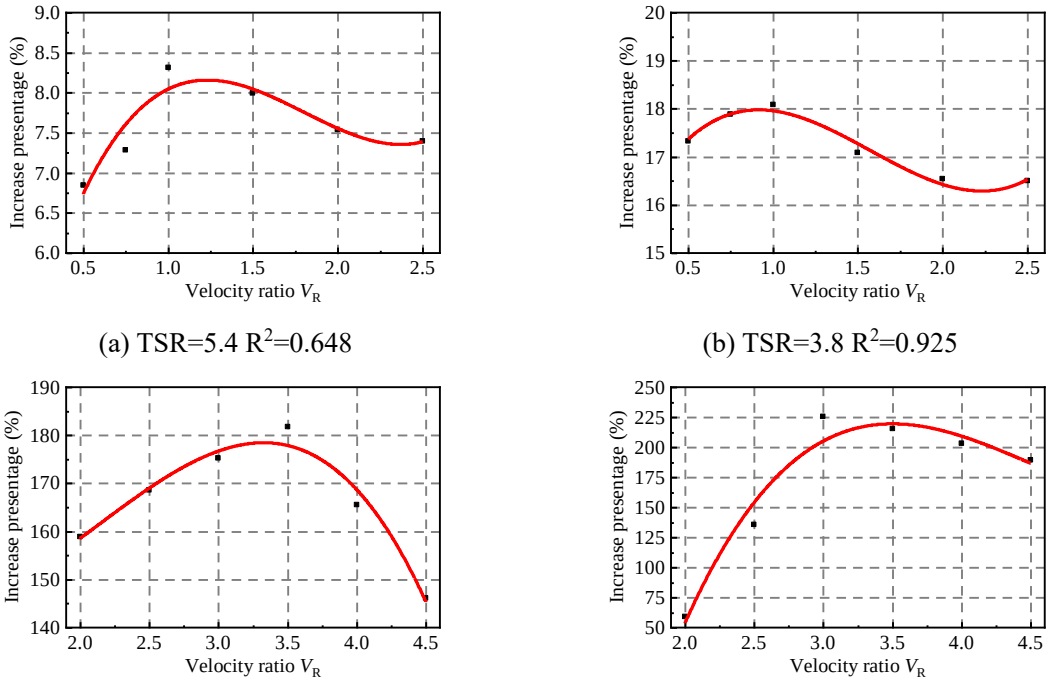

(a) TSR=5.4 R^2=0.648 (b) TSR=3.8 R^2=0.925

(c) TSR=2.9 R^2=0.912 (d) TSR=1.9 R^2=0.895

Fig.8. Correlation curves between increment percent and V_R at different TSR.

5.4 Flow field morphology with BLS control

Since the control mechanism of BLS cannot be known by power increment alone, in order to further analyze the control mechanism of BLS control, the surface streamline, velocity cloud of blade section and pressure coefficient of clean blade and BLS blade are analyzed.

(a) clean (b) L3 (c) L6 (d) L9

Fig.9. The surface streamline of the clean blades compared with L3, L6 and L9 blades under U_∞=7 m/s.

(a) clean (b) S3 (c) S6 (d) S9

Fig.10. The surface streamline of the clean blades compared with S3, S6 and S9 blades under U_∞=10 m/s.

Fig.9 shows the surface streamline of the clean blades compared with L3, L6 and L9 blades under U_∞=7 m/s. As can be seen from the figure, there is almost no flow separation on the suction surface of clean blade, and only a small part of trailing edge has non-attachment phenomenon. At this point, BLS control has no significant improvement effect on surface flow of blade. Fig.10 shows the surface streamline of the clean blades compared with S3, S6 and S9 blades under U_∞=10 m/s. As can be seen from the figure, the clean blade separation occurs around the middle. The area controlled by BLS can be significantly improved by making the streamline fit the wall and improving the blade flow. When BLS_1 shuts down and BLS_2 works, the flow in the A_2 is significantly improved, but the flow in the A_1 is more complex, which leads to high load fluctuations and is detrimental to the life of the blade. With both BLS_1 and BLS_2 work, the overall blade flow is improved, with only a small flow separation occurs at the root.

(a) clean (b) M3 (c) M6 (d) M10

Fig.11. The surface streamline of the clean blades compared with M3, M6 and M10 blades under U_∞=13 m/s.

(a) clean (b) H3 (c) H6 (d) H9

Fig.12. The surface streamline of the clean blades compared with H3, H6 and H10 blades under U_∞=20 m/s.

Fig.11 shows the surface streamline of the clean blades compared with M3, M6 and M10 blades under U_∞=13 m/s. As can be seen from Fig.11a, when U_∞=13 m/s, the clean blade surface presents a large-scale flow separation. At this time, the effect of BLS_1 control alone is not obvious, while BLS_2 control alone can improve the flow in A_2. When BLS_1 and BLS_2 work together, the overall flow of blade is improved, indicating that BLS control is not only effective in small-scale flow separation, but also significant in large-scale flow separation. Fig.12 shows the surface streamline of the clean blades compared with H3, H6 and H10 blades under U_∞=20 m/s. It can be seen from the figure that the result is similar to that of U_∞=13 m/s. However, when U_∞=20 m/s, the flow separation is further intensified, so the combined work of BLS_1 and BLS_2 cannot completely inhibit the separation, so there are still small areas of flow separation in the root and tailing edge of blade tip.

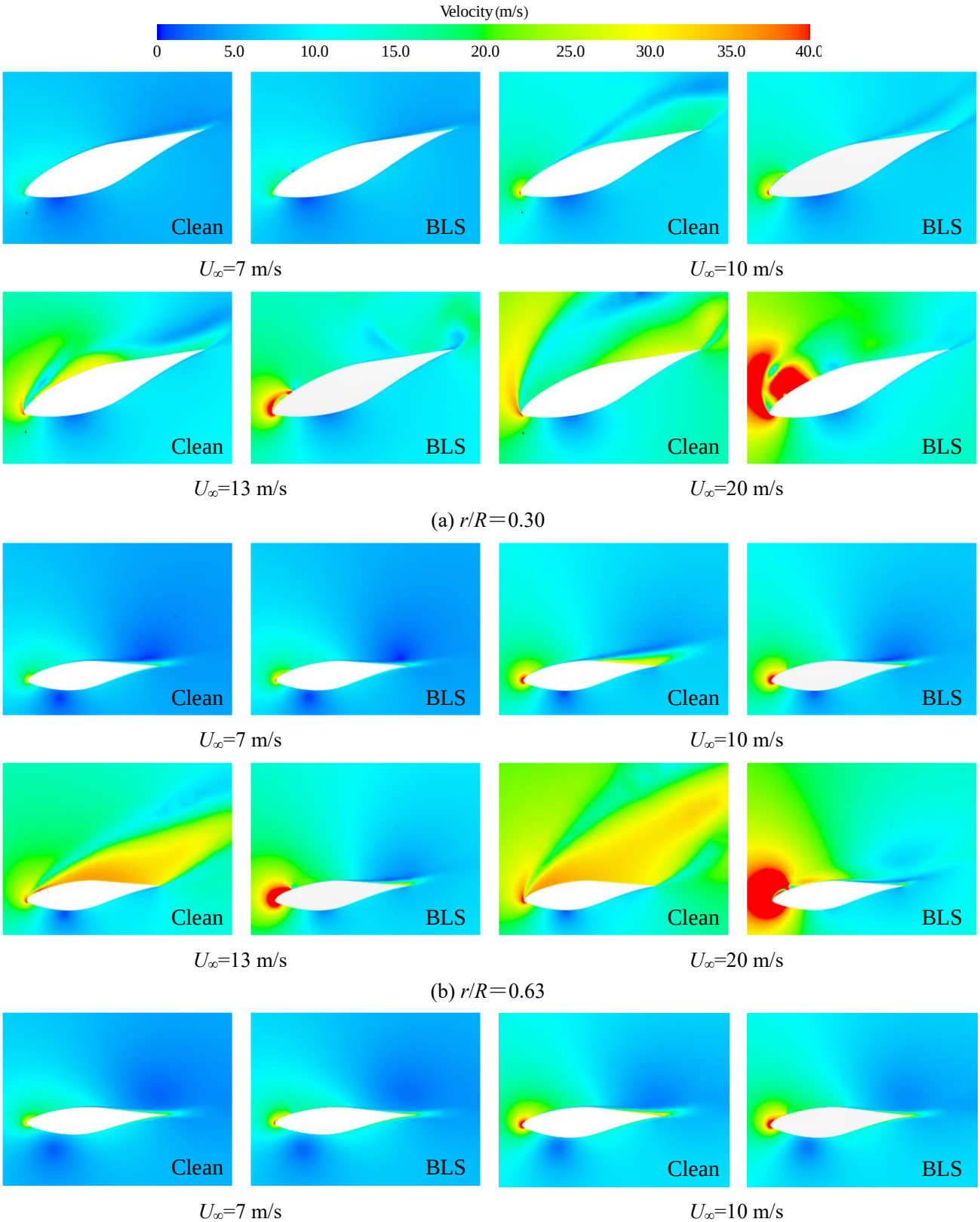

U_∞=7 m/s U_∞=10 m/s

U_∞=13 m/s U_∞=20 m/s

(a) r/R=0.30

Clean BLS Clean BLS

U_∞=7 m/s U_∞=10 m/s

Clean BLS Clean BLS

U_∞=13 m/s U_∞=20 m/s

(b) r/R=0.63

Clean BLS Clean BLS

U_∞=7 m/s U_∞=10 m/s

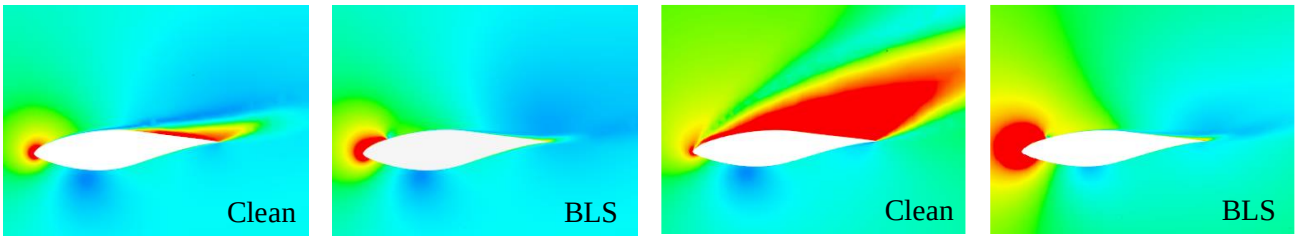

U_∞=13 m/s U_∞=20 m/s

(c) r/R=0.95

Fig.13. Velocity flow field of blade sections with (L9, S9, M10 & H9) and without BLS control.

In order to further deepen the understanding of BLS control, the velocity flow field of each section of the blade is demonstrated, while its pressure coefficients are plotted. Fig.13 shows the velocity flow field of blade sections with and without BLS control under U_∞=7, 10, 13 and 20 m/s. As can be seen from the figure, when U_∞=7 m/s, each section of the blade almost has no stall zone, and the BLS control effect is not obvious at this time. With the decrease of TSR, the flow separation gradually appeared on the blade surface, when U_∞=10 m/s, there is a small stall zone at trailing edge of each section of the blade. After adopting BLS control, the stall is significantly improved.

As can be seen from Fig.13, when U_∞=13 m/s, there are large stall areas at r/R=0.30, 0.47, 0.63 and 0.80. After adopting BLS control, the low-velocity fluid in the separation zone is removed, and the formation and development of leading edge vortices are inhibited, thus the flow field is significantly improved. Combined with Fig.14, it can be seen that the BLS control can effectively increase the pressure difference between the suction surface and the pressure surface, which significantly raises the peak negative pressure at the leading edge, shifts the airfoil flow separation point back, reduces the range of separation vortices over a large area and mitigates the effect of stall on the aerodynamic performance of the blade. Compared with high TSR, the BLS control effect is particularly obvious at low to medium TSR.

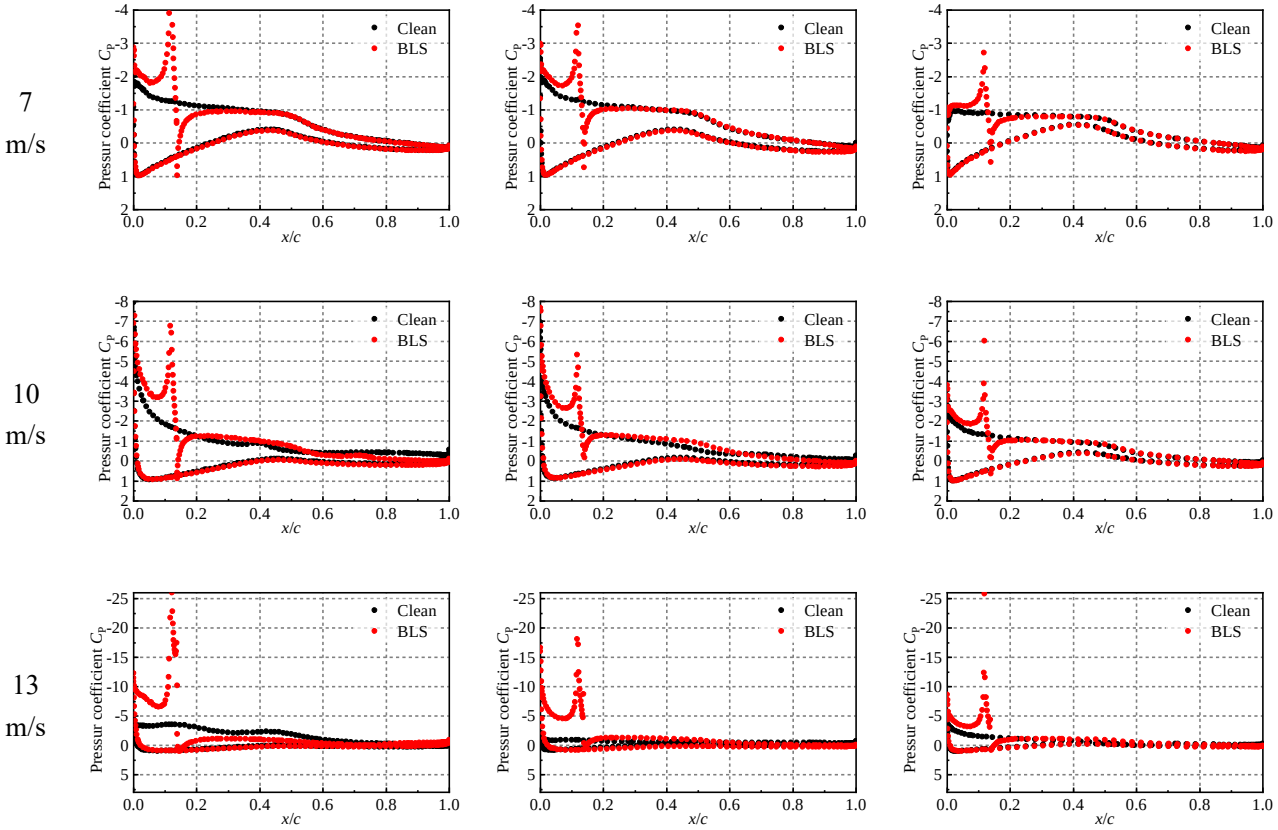

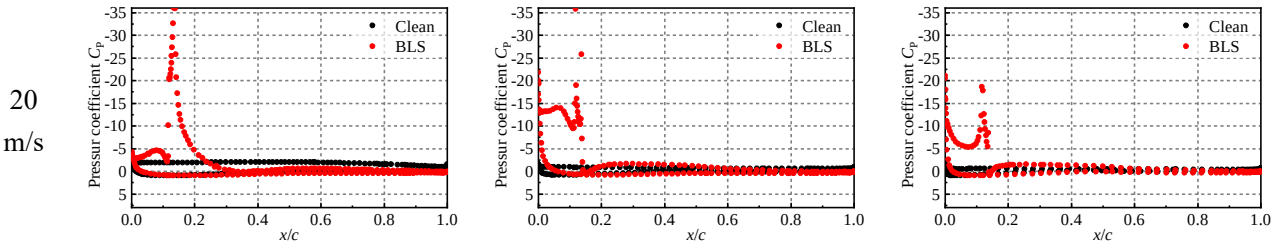

(a) r/R=0.30 (b) r/R=0.63 (c) r/R=0.95

Fig.14. Comparison of pressure coefficients of each section.

5.5 Influence of the BLS working angle

In addition to the BLS momentum coefficient, the BLS working angle also has an important influence on the control efficiency. Therefore, the effect of BLS working angle on control efficiency is further analyzed by dividing the working angle into nine cases at 20° intervals, as can be seen in Fig.15a. When the C_μ of BLS_1 and BLS_2 is 0.16 under U_∞=13 m/s, the case Q7 is analyzed. Fig.15b shows the variation of power increment for different working angles.

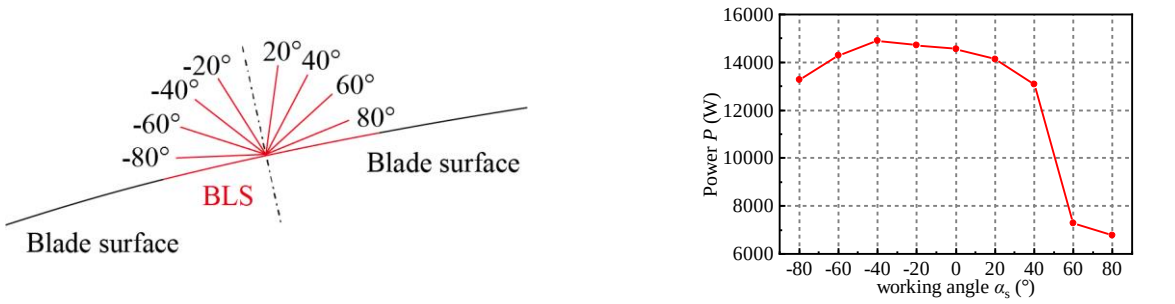

(a) Different working angles

(b) The power of wind turbine for different working angles

Fig.15. The variation of power for different working angles.

As can be seen from Fig.15b, the BLS control obtains higher power at -40° and -20° working angle than at 0°, which means that the control efficiency of BLS control is enhanced at these two angles. Among them, the power is highest at -40°, and we believe that BLS can achieve the highest control efficiency at working angle of about -40°. Combined with Fig.16, it can be seen that under the excessive forward angle, the angle of BLS suction is too large (nearly 180°) with the incoming flow, resulting in the appearance of additional irregular vortices. At this time, BLS control has little effect on the improvement of flow field, and even has negative benefit.

(a) Clean (b) BLS(α_s= 80°)

Fig.16. Flow field at r/R=0.63 for BLS working angle of 80°.

6. Conclusion

This research evaluates the possible benefits of applying BLS on HAWT blades. In fact, in the field of aircraft, BLS is considered as a simple and effective method to improve lift-to-drag ratio of the airfoil and reduce the flow

separation. Within the wind energy market and research, the flow control of HAWT is experiencing a new interest.

In this research, a lot of work has been done in pre-validation in order to better display the flow field characteristics. Based on the experience of researchers, the SST k-ω turbulence model is considered to be the most suitable for NREL Phase VI simulations. In addition, the computational burden of the 3D flow field is very high, and in this research, the effect of hub and tower is neglected to simulate a single blade while ensuring the computational accuracy. Although the CFD results overestimate the stall speed at the leaf root at U_∞=15 m/s and r/R=0.30, the overall results show that our CFD simulations have reliable results.

First, we evaluated the effect of the BLS arranged at the leading edge of the airfoil under 2D simulations. The dynamic mode decomposition is used to decompose the flow field of clean airfoil and BLS airfoil into four modes to deeply analyze the mechanism of BLS control. Subsequently, the effect of BLS on the HAWT blade is analyzed by selecting four kinds of incoming wind speeds (U_∞=7, 10, 13 and 20 m/s). The location of BLS was fixed at 0.15c from the leading edge, and the effect of power increment and flow field improvement on the HAWT blade was analyzed by changing the momentum coefficient of BLS. In addition, we provide the relevant equations for these four TSRs in a specific V_R range. Finally, since the working angle of BLS is another factor affecting the control efficiency, this research further analyzes the effect of working angle on the control efficiency by dividing the working angle by 20° interval. The conclusions are as follows:

(1) The BLS control can significantly reduce the range of stall area by inhaling low-momentum fluid in the boundary layer and making the fluid better attached to the suction surface. Meanwhile, the analysis of the characteristic value unit circle shows that the use of BLS can effectively increase the stability of the flow field.

(2) The BLS control can effectively increase the pressure difference between the suction surface and the pressure surface, significantly increasing the peak negative pressure at the leading edge, shifting the airfoil flow separation point backwards, reducing the separation vortex range over a large area and mitigating the effect of stall on the aerodynamic performance of the blade.

(3) At high TSRs, the BLS control has no significant improvement effect on surface flow of blade because there is almost no flow separation on blade surface. With the decrease of the TSR, the flow separation area of the blade increases. At low to medium TSRs, when the surface flow of blade is complex, the use of BLS control can significantly improve the surface flow of blade.

(4) When only the root part of the blade is controlled, the gain is negative after considering the energy consumption of BLS. The BLS control at the middle of the blade and the tip plays the main role. However, the amount of gain obtained when both regions are controlled simultaneously is not simply superimposed, but has a greater increment, which indicates that the power increment is not only the result of single region control, but the result of two control regions together.

(5) The BLS control can effectively improve the power capability of HAWT. Considering the BLS energy consumption comprehensively, the maximum increment of power can be 207.36 W under U_∞=7 m/s and 1028.26 W under U_∞=10 m/s, which is 8.32% and 18.08% higher than the clean blade. The maximum increment of power can be 8730.10 W under U_∞=13 m/s and 7642.14 W under U_∞=20 m/s, which is 181.71% and 225.56% higher than the clean blade.

(6) The working angle of BLS should be shifted towards the leading edge of the airfoil to eliminate the separation bubble in advance, thus inhibiting the formation and development of shedding vortices more effectively. It is concluded that the α_s of -40° perform the best energy production.

In practical engineering applications, a separate gas source for BLS control should be considered. However, further studies are needed to better assess the benefits of BLS for HAWT. For example, the placement of these BLS means an increase in the extra weight of the blades, as well as an increase in the stress the blades are subjected to,

which inevitably has an impact on the cost of wind turbine construction. However, after actual layout, the working angle of BLS cannot be accurately determined due to technical limitations, and we suggest an acceptable working angle of 0° to -40°.

7. Future work

This paper mainly studied the influence of different BLS control momentum coefficients on HAWT aerodynamic performance and the contribution of the two control regions to power increment under four TSR from high to low. The following may be undertaken in the future:

(1) In this research, the BLS control is fixed on the suction surface at a position 0.15c from the leading edge, and the effect of different arrangement positions on the power increment of the HAWT can be studied.

(2) In this research, the control area is divided into two regions, and the control area can be further subdivided.

(3) Considering only the single BLS, different number of BLS with different momentum coefficients can be arranged for different positions of blades to achieve more accurate flow control.

(4) The BLS control in this research is constant, and unsteady control may have different effects on power saving and noise reduction.

Acknowledgements

The authors would like to acknowledge the support of National Natural Science Foundation of China (Grand No. 51976131, 52006148 and 52106262).

References

[1] Egli F, Steffen B, Schmidt T S. Learning in the financial sector is essential for reducing renewable energy costs [J]. Nature Energy, 2019, 4(10): 835-836.

[2] Li L, Ren X, Yang Y, et al. Analysis and recommendations for onshore wind power policies in China [J]. Renewable and Sustainable Energy Reviews, 2018, 82: 156-167.

[3] Sun X, Zhang L, Huang D, et al. Understanding the performance of an oscillating-wing wind power generator over a wide range of operating parameters [J]. International Journal of Energy Research, 2018, 42(2): 776-789.

[4] Miao W P, Li C, Pavesi G, et al. Investigation of wake characteristics of a yawed HAWT and its impacts on the inline downstream wind turbine using unsteady CFD [J]. Journal of Wind Engineering and Industrial Aerodynamics, 2017, 168: 60-71.

[5] Global Wind Report 2022 [EB/OL]. https://gwec.net/global-wind-report-2022/

[6] Wang P L, Liu Q S, Li C, et al. Effect of trailing edge dual synthesis jets actuator on aerodynamic characteristics of a straight-bladed vertical axis wind turbine [J]. Energy, 2022, 238: 121792.

[7] Shukla V, Kaviti A K. Performance evaluation of profile modifications on straight-bladed vertical axis wind turbine by energy and Spalart Allmaras models [J]. Energy, 2017, 126: 766-95.

[8] Li Q, Maeda T, Kamada Y, et al. Effect of number of blades on aerodynamic forces on a straight-bladed Vertical Axis Wind Turbine [J]. Energy, 2015, 90: 784-95.

[9] Manerikar S S, Damkale S R, Havaldar S N, et al. Horizontal axis wind turbines passive flow control methods: a review [C]//IOP Conference Series: Materials Science and Engineering. IOP Publishing, 2021, 1136(1): 012022.

[10] Dollinger C, Balaresque N, Sorg M, et al. IR thermographic visualization of flow separation in applications with low thermal contrast [J]. Infrared physics & technology, 2018, 88: 254-264.

[11] Bangga G, Lutz T, Krämer E. Root flow characteristics and 3D effects of an isolated wind turbine rotor [J]. Journal of Mechanical Science and Technology, 2017, 31(8): 3839-3844.

[12] Liu Q S, Miao W P, Li C, et al. Effects of trailing-edge movable flap on aerodynamic performance and noise characteristics of VAWT [J]. Energy, 2019, 189.

[13] Rose J, Natarajan S G, Gopinathan V T. Biomimetic flow control techniques for aerospace applications: A comprehensive review [J]. Reviews in Environmental Science and Bio/Technology, 2021, 20(3): 645-677.

[14] Zhu H, Hao W, Li C, et al. A critical study on passive flow control techniques for straight-bladed vertical axis wind turbine [J]. Energy, 2018, 165: 12-25.

[15] Li J, Ji L. Efficient design method for applying vortex generators in turbomachinery [J]. Journal of Turbomachinery, 2019, 141(8).

[16] Dadamoussa A, Boualem K, Yahiaoui T, et al. Numerical investigation of flow on a darrieus Vertical Axis Wind Turbine blade with vortex generators [J]. International Journal of Fluid Mechanics Research, 2020, 47(1).

[17] Mohamed O S, Ibrahim A A, Etman A K, et al. Numerical investigation of Darrieus wind turbine with slotted airfoil blades [J]. Energy Conversion and Management: X, 2020, 5: 100026.

[18] Zhu H T, Hao W X, Li C, et al. Numerical study of effect of solidity on vertical axis wind turbine with Gurney flap [J]. Journal of Wind Engineering & Industrial Aerodynamics, 2019, 186.

[19] Hao W, Bashir M, Li C, et al. Flow control for high-solidity vertical axis wind turbine based on adaptive flap [J]. Energy Conversion and Management, 2021, 249: 114845.

[20] Mayer Y D, Lyu B, Jawahar H K, et al. A semi-analytical noise prediction model for airfoils with serrated trailing edges [J]. Renewable Energy, 2019, 143: 679-691.

[21] Wang Y, Li G, Shen S, et al. Investigation on aerodynamic performance of horizontal axis wind turbine by setting micro-cylinder in front of the blade leading edge [J]. Energy, 2018, 143: 1107-1124.

[22] Moshfeghi M, Shams S, Hur N. Aerodynamic performance enhancement analysis of horizontal axis wind turbines using a passive flow control method via split blade [J]. Journal of Wind Engineering and Industrial Aerodynamics, 2017, 167: 148-159.
[23] Zhang Y, Ramdoss V, Saleem Z, et al. Effects of root Gurney flaps on the aerodynamic performance of a horizontal axis wind turbine [J]. Energy, 2019, 187: 115955.
[24] Zhu H T, Hao W X, Li C, et al. Simulation on flow control strategy of synthetic jet in an vertical axis wind turbine [J]. Aerospace Science and Technology, 2018, 77.
[25] Abdollahzadeh M, Pascoa J C, Oliveira P J. Comparison of DBD plasma actuators flow control authority in different modes of actuation [J]. Aerospace science and technology, 2018, 78: 183-196.
[26] Makarewicz R, Gołębiewski R. The influence of a low level jet on the thumps generated by a wind turbine [J]. Renewable and Sustainable Energy Reviews, 2019, 104: 337-342.
[27] Corsini, Alessandro, Delibra, et al. The application of sinusoidal blade-leading edges in a fan-design methodology to improve stall resistance [J]. Proceedings of the Institution of Mechanical Engineers, 2014, 228(3).
[28] Abdulrahim A, Anık E, Ostovan Y, et al. Effects of tip injection on the performance and near wake characteristics of a model wind turbine rotor[J]. Renewable Energy, 2016, 88: 73-82.
[29] Aono H, Fukumoto H, Abe Y, et al. Separated flow control of small horizontal-axis wind turbine blades using dielectric barrier discharge plasma actuators [J]. Energies, 2020, 13(5): 1218.
[30] Mohammadi M, Maghrebi M J. Improvement of wind turbine aerodynamic performance by vanquishing stall with active multi air jet blowing [J]. Energy, 2021, 224: 120176.
[31] Shi F, Xu Y, Sun X. Numerical investigation of active flow control with co-flowing jet in a horizontal axis wind turbine [J]. Wind Engineering, 2021, 45(5): 1101-1122.[32] Prandtl L. Über Flussigkeitsbewegung bei sehr kleiner Reibung [J]. Verhandl. III, Internat. Math.-Kong., Heidelberg, Teubner, Leipzig, 1904, 1904: 484-491.
[33] Kulkarni R S, Rohit B, Lokanatha V, et al. Understanding boundary layer suction and its effect on wings-A review [C]//IOP Conference Series: Materials Science and Engineering. IOP Publishing, 2018, 376(1): 012030.
[34] Kumar B R. Aerodynamic design optimization of an automobile car using computational fluid dynamics approach [J]. Australian Journal of Mechanical Engineering, 2021, 19(5): 495-501.
[35] Wang Z, Gursul I. Lift enhancement of a flat-plate airfoil by steady suction [J]. AIAA Journal, 2017, 55(4): 1355-1372.
[36] Lei J, Liu Q, Li T. Suction control of laminar separation bubble over an airfoil at low Reynolds number [J]. Proceedings of the Institution of Mechanical Engineers, Part G: Journal of Aerospace Engineering, 2019, 233(1): 81-90.
[37] Arunraj R., Logesh K., Balaji V., et al. Experimental investigation of lift enhancement by suction-assisted delayed separation of the boundary layer on NACA 0012 airfoil [J]. International Journal of Ambient Energy, 2019, 40(3): 243-247.
[38] Morgulis N, Seifert A. Fluidic flow control applied for improved performance of Darrieus wind turbines [J]. Wind Energy, 2016, 19(9): 1585-1602.
[39] Rezaeiha A, Montazeri H, Blocken B. Active flow control for power enhancement of vertical axis wind turbines: leading-edge slot suction [J]. Energy, 2019, 189: 116131.
[40] Rezaeiha A, Montazeri H, Blocken B. CFD analysis of dynamic stall on vertical axis wind turbines using Scale-Adaptive Simulation (SAS): Comparison against URANS and hybrid RANS/LES [J]. Energy Conversion and Management, 2019, 196: 1282-1298.
[41] Rezaeiha A, Montazeri H, Blocken B. CFD investigation of separation control on a vertical axis wind turbine: steady and unsteady suction [C]//Journal of Physics: Conference Series. IOP Publishing, 2020, 1618(5): 052019.

[42] Sun J, Sun X, Huang D. Aerodynamics of vertical-axis wind turbine with boundary layer suction–Effects of suction momentum [J]. Energy, 2020, 209: 118446.
[43] Sun J, Huang D. Numerical investigation of boundary layer suction control positions on airfoils for vertical-axis wind turbine [J]. Journal of Mechanical Science and Technology, 2021, 35(7): 2903-2914.
[44] Arnold B, Lutz T, Krämer E. Design of a boundary-layer suction system for turbulent trailing-edge noise reduction of wind turbines [J]. Renewable Energy, 2018, 123: 249-262.
[45] Arnold B, Lutz T, Krämer E, et al. Wind-turbine trailing-edge noise reduction by means of boundary-layer suction [J]. AIAA Journal, 2018, 56(5): 1843-1854.
[46] Moussavi S A, Ghaznavi A. Effect of boundary layer suction on performance of a 2 MW wind turbine [J]. Energy, 2021, 232: 121072.
[47] Iswahyudi S, Wibowo S B. Effect of blade tip shapes on the performance of a small HAWT: An investigation in a wind tunnel [J]. Case Studies in Thermal Engineering, 2020, 19: 100634.
[48] Ghasemian M, Nejat A. Aerodynamic noise prediction of a horizontal axis wind turbine using improved delayed detached eddy simulation and acoustic analogy [J]. Energy Conversion and Management, 2015, 99: 210-220.
[49] Wang Y, Li G, Shen S, et al. Investigation on aerodynamic performance of horizontal axis wind turbine by setting micro-cylinder in front of the blade leading edge [J]. Energy, 2018, 143: 1107-1124.
[50] Regodeseves P G, Morros C S. Unsteady numerical investigation of the full geometry of a horizontal axis wind turbine: Flow through the rotor and wake [J]. Energy, 2020, 202: 117674.
[51] Hand M M, Simms D A, Fingersh L J, et al. Unsteady aerodynamics experiment phase VI: wind tunnel test configurations and available data campaigns [R]. National Renewable Energy Lab., Golden, CO. (US), 2001.
[52] Duque E P N, Burklund M D, Johnson W. Navier-Stokes and comprehensive analysis performance predictions of the NREL phase VI experiment [J]. J. Sol. Energy Eng., 2003, 125(4): 457-467.
[53] Sørensen N N, Michelsen J A, Schreck S. Navier–Stokes predictions of the NREL phase VI rotor in the NASA Ames 80 ft× 120 ft wind tunnel [J]. Wind Energy: An International Journal for Progress and Applications in Wind Power Conversion Technology, 2002, 5(2-3): 151-169.
[54] Jones W P, Launder B E. The calculation of low-Reynolds-number phenomena with a two-equation model of turbulence [J]. International Journal of Heat and Mass Transfer, 1973, 16(6): 1119-1130.
[55] Wilcox D C. Reassessment of the scale-determining equation for advanced turbulence models [J]. AIAA journal, 1988, 26(11): 1299-1310.
[56] Rocha P A C, Rocha H H B, Carneiro F O M, et al. k–ω SST (shear stress transport) turbulence model calibration: A case study on a small scale horizontal axis wind turbine [J]. Energy, 2014, 65: 412-418.
[57] Wang T. A brief review on wind turbine aerodynamics [J]. Theoretical and Applied Mechanics Letters, 2012, 2(6): 062001.
[58] Bai C J, Wang W C. Review of computational and experimental approaches to analysis of aerodynamic performance in horizontal-axis wind turbines (HAWTs) [J]. Renewable and Sustainable Energy Reviews, 2016; 63: 506-519.
[59] Menter F R. Two-equation eddy-viscosity turbulence models for engineering applications [J]. AIAA journal, 1994, 32(8): 1598-1605.
[60] Tachos N S, Filios A E, Margaris D P. A comparative numerical study of four turbulence models for the prediction of horizontal axis wind turbine flow [J]. Proceedings of the Institution of Mechanical Engineers, Part C: Journal of Mechanical Engineering Science, 2010, 224(9): 1973-1979.
[61] Chow R, Van Dam C P. Verification of computational simulations of the NREL 5 MW rotor with a focus on inboard flow separation [J]. Wind Energy, 2012, 15(8): 967-981.

[62] Roache P J. Perspective: a method for uniform reporting of grid refinement studies [J]. 1994.
[63] Roache P J. Quantification of uncertainty in computational fluid dynamics [J]. Annual review of fluid Mechanics, 1997, 29(1): 123-160.
[64] Beabpimai W, Chitsomboon T. Numerical study of effect of blade twist modifications on the aerodynamic performance of wind turbine [J]. International Journal of Renewable Energy Development, 2019, 8(3): 285-292.
[65] Abdelwaly M, El-Batsh H, Hanna M B. Numerical study for the flow field and power augmentation in a horizontal axis wind turbine [J]. Sustainable Energy Technologies and Assessments, 2019, 31: 245-253.
[66] Taira K, Brunton S L, Dawson S T M, et al. Modal analysis of fluid flows: An overview [J]. Aiaa Journal, 2017, 55(12): 4013-4041.